

Flux-coupled tunable superconducting resonator

Juliang Li^{1,*}, Pete Barry², Tom Cecil¹, Marharyta Lisovenko¹, Volodymyr Yefremenko,¹
Gensheng Wang,¹ Serhii Kruhlov^{1,3}, Goran Karapetrov³, and Clarence Chang^{1,4,5}


¹*Argonne National Laboratory, 9700 South Cass Ave., Lemont, Illinois 60439, USA*

²*Cardiff University, Cardiff CF10 3AT, United Kingdom*

³*Department of Physics, Drexel University, 3141 Chestnut St., Philadelphia, Pennsylvania 19104, USA*

⁴*University of Chicago, 5640 South Ellis Ave., Chicago, Illinois 60637, USA*

⁵*Kavli Institute for Cosmological Physics, University of Chicago, 5640 South Ellis Ave., Chicago, Illinois 60637, USA*

 (Received 19 December 2023; revised 27 February 2024; accepted 24 June 2024; published 30 July 2024)

We present a design and implementation of a frequency-tunable superconducting resonator. The resonance frequency tunability is achieved by flux-coupling a superconducting LC loop to a current-biased feedline; the resulting screening current leads to a change of the kinetic inductance and shift in the resonance frequency. The thin-film aluminum resonator consists of an interdigitated capacitor and thin line inductors forming a closed superconducting loop. The magnetic flux from the nearby niobium current feedline induces Meissner shielding currents in the resonator loop leading to a change in the kinetic part of the total inductance of the resonator. We demonstrate continuous frequency tuning within 160 MHz around the resonant frequency of 2.7 GHz. We show that: (1) frequency up-conversion is achieved when a kilohertz ac modulation signal is superimposed onto the dc bias resulting in sidebands to the resonator tone; (2) three-wave mixing is attained by parametrically pumping the nonlinear kinetic inductance using a strong rf pump signal in the feedline. The simple architecture is amenable to large-array multiplexing and on-chip integration with other circuit components. The concept could be applied in flux magnetometers, up-converters, and parametric amplifiers operating above 4 K when alternative high-critical-temperature material with high kinetic inductance is used.

DOI: [10.1103/PhysRevApplied.22.014080](https://doi.org/10.1103/PhysRevApplied.22.014080)

I. INTRODUCTION

With their high quality factors and easy planar fabrication, superconducting resonators have found wide use in applications such as astronomical detectors [1–3], spin resonance techniques [4,5], and superconducting quantum computing [6,7]. Tunable superconducting resonators are attractive as they provide an effective platform for applications where fine frequency tuning is required to achieve a desired coupling strength. Applications include quantum memories [8] and interfaces with various forms of excitation such as phonons [9,10], photons [11–14], and electrical charges [15]. Tunable superconducting resonators are also applied in spin systems for addressing spin transitions and conducting dynamical switching between them: nitrogen-vacancy (N-V) centers in diamond [16,17], molecular spins [18–20], yttrium iron garnet (YIG), and magnon-based systems [21–24]. Furthermore, tunable resonators with three-wave mixing capability offer a platform for designing new quantum sensing protocols [25–30].

Tunable resonators have also been developed for characterizing high-kinetic-inductance superconducting thin films [31].

Common approaches for realizing frequency-tunable microwave resonators include the use of Josephson junctions (JJs) [32–37], nanoconstriction superconducting quantum interference device (SQUID) loop [38], magnetic field reorientation [39], and high-kinetic-inductance superconducting wires [40–47]. The large nonlinear inductance of JJs offers large frequency tuning range and tuning speed. However, JJ devices require low magnetic fields and the oxidation barrier in the junction degrades the resonator quality factor. They also have relatively low saturation power due to their limited critical current. On the other hand, high-kinetic-inductance wires can be easily fabricated because of their simple geometries and are suitable for higher operating temperature and power arising from their higher critical temperature (T_c) and critical current (I_c) compared with JJs. Tuning the kinetic inductance is possible by changing the quasiparticle density in the superconductor, which can be realized by applying a current through the material, applying an external magnetic field,

*Contact author. juliang.li@anl.gov

or by varying the film temperature. Changing the current density is a common approach and requires dc current biasing of the inductor, which has typically been realized through direct coupling of the bias current. Here, we present an architecture using a superconducting resonator made from an aluminum thin film where this current couples inductively to proximal a niobium feedline. Niobium is being used for the feedline because of a larger superconducting critical current than aluminum.

The paper is organized as follows. In Sec. II we discuss the operating principles and design of the resonator along with its fabrication process. Section III demonstrates flux coupling of both low-frequency (~ 10 kHz) and high-frequency (~ 5 GHz) ac signals which can be used for frequency up-conversion and three-wave mixing processes. In Sec. IV we describe operating the resonator as a parametric amplifier and demonstrate preliminary results showing gain for both degenerate and nondegenerate three-wave pumping. We conclude in Sec. V and discuss potential changes to the resonator to improve the frequency tunability and flux coupling strength.

II. RESONATOR DESIGN

Our tunable resonator design is illustrated in Fig. 1. Two inductors are placed in parallel with an interdigitated capacitor in the middle. The inductors and the two straight edges of the capacitor form a superconducting loop that can carry a continuous circulating Meissner currents. The applied current to the niobium readout line via dc “in” and “out” ports generates a magnetic field and the corresponding total magnetic flux imposed on the loop given by

$$\Phi_{\text{dc}} = w \frac{\mu_0 I_{\text{dc}}}{2\pi} \log\left(\frac{r_2}{r_1}\right), \quad (1)$$

where I_{dc} is the dc current supplied through the readout line and Φ_{dc} is the resulting magnetic flux threading the superconducting loop. Here r_1 and r_2 (shown in Fig. 2) are the distances from the readout line to the two opposite edges of our square resonator loop that are parallel to the readout line, and w is the width of the square loop parallel to the readout line.

Flux quantization in the closed superconducting loop necessitates a circulating or screening current (I_{sc}) given by

$$L_{\text{self}} \times I_{\text{sc}} + \Phi_{\text{dc}} = m\Phi_0, \quad (2)$$

where L_{self} is the self-inductance of the superconducting loop, Φ_0 is the magnetic flux quantum, and m is integer of flux quanta present in the superconducting loop. This screening current will modify the kinetic inductance with

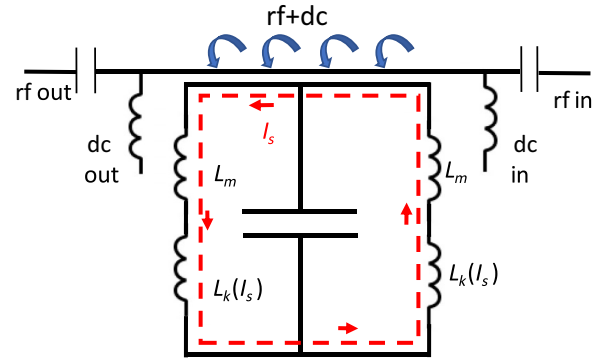


FIG. 1. Equivalent circuit of the flux biased tunable resonator. In the center is the interdigitated capacitor and the inductor carries both geometric (L_o) and kinetic (L_k) inductance. The rf and dc currents are combined through bias tees and fed through the readout line. By Eq. (2), magnetic flux generated from dc current in the readout line (wide blue arrow bar) excites a screening current I_{sc} (red dashed line) in the superconducting loop.

relationship given by

$$L_k \approx L_{k0} \left[1 + \left(\frac{I_{\text{sc}}}{I^*} \right)^2 \right], \quad (3)$$

where L_{k0} is the intrinsic kinetic inductance at zero current, and I^* sets the characteristic scale of the nonlinearity and has a value close to the superconducting critical current I_c [48,49].

Starting from the design geometry of our resonator, we derive the relative frequency shift as a function of dc bias current I_{dc} as

$$\frac{\Delta f}{f_0} = \frac{\alpha(-MI_{\text{dc}} + m\Phi_0)^2}{2L_{\text{self}}^2 I^{*2}}, \quad (4)$$

where α is kinetic inductance participation ratio and M is the mutual inductance between the readout line and the superconducting loop. Details of the calculation could be found in Appendix A.

Figure 2 shows the physical layout of the frequency tunable microwave resonator. The resonator consists of a central set of interdigitated fingers, which acts as the capacitor, and with both ends connected by narrow lines which act as inductors. The resonator is placed $2 \mu\text{m}$ away from a Nb microstrip readout line. The gap provides rf coupling to the feedline which is used for readout of the resonator via a microwave probe tone. Detailed parameters of the design can be found in Table I. Device fabrication is carried out using e-beam lithography and single-layer resist lift-off processes. The process begins with a low-resistivity prime silicon wafer with native oxide. The wafer is coated with a 200-nm-thick layer of PMMA 950 A4 resist. The resist is exposed in a JEOL JBX-8100FS e-beam writer at

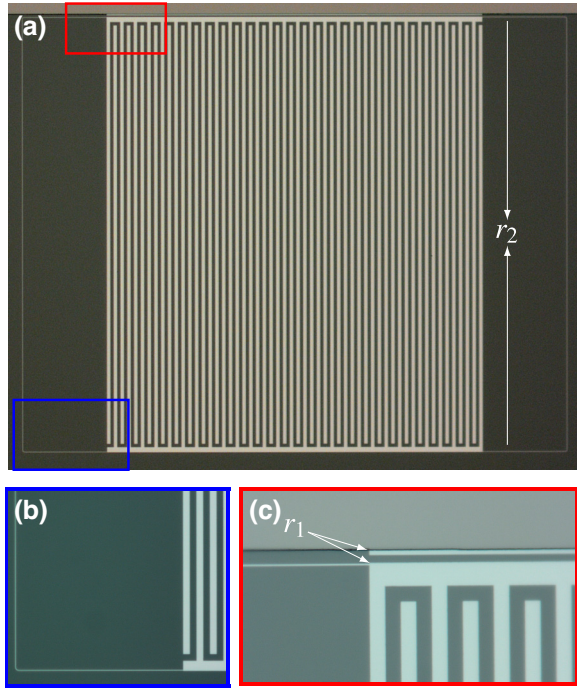


FIG. 2. (a) The tunable resonator. Lighter color marks the lumped LC resonator and the readout line that carries both the rf and dc signals. Darker color is the silicon substrate. In the center is the interdigitated capacitor and the narrow lines on both sides are the inductors. Here r_2 is the distance from the furthest end of the loop to the readout line that is used for flux calculation. (b) Enlarged view of the inductor with width of 400 nm and interdigitated capacitor in the blue rectangle of (a). (c) Coupling of the LC resonator to the readout line corresponding to the area outlined by the red square of (a). Darker color is the Nb readout line and the lighter color is part of the LC resonator. The coupling quality factor Q_c for the resonator is determined by the gap between the resonator and the readout line, which we designed to be 2 μm . Here r_1 is the gap between the readout line and the loop.

a dose of 720 mJ/cm^2 and developed in a methyl isobutyl ketone (MIBK) and isopropanol (IPA) mix (1:3). Next, a 30-nm-thick Al layer is deposited via sputtering at a base pressure below 5×10^{-8} Torr. The wafer is then placed in a Microposit 1165 remover to lift-off the residual Al stack. The readout line is fabricated in a second step with the same lift-off process used on 300 nm of Nb. Two resonators are patterned with inductor widths of 400 nm and 300 nm and the same capacitor dimensions.

The resonator chip is measured in a dilution refrigerator with base temperature of 30 mK. The measured zero-bias resonant frequency for the two resonators, with inductor line width of 400 and 300 nm, are 3.148 and 2.705 GHz, respectively. Figure 3 shows the relative resonance frequency shift $\Delta f/f_o = (f - f_o)/f_o$ for the two resonators as a function of applied dc current bias. Over 160 MHz frequency shift is observed for the 2.7 GHz resonator while

TABLE I. Parameters of the flux biased resonator.

Capacitor (aluminum):	
Finger width (μm)	4
Finger length (μm)	480
Gap between fingers (μm)	4
Gap between finger and capacitor end (μm)	4
Number of finger pairs	28
Length of capacitor end (μm)	500
Width of capacitor end (μm)	6
Inductor (aluminum):	
Width (nm)	300, 400
Length (μm)	700
f_o (GHz)	2.705, 3.148
Q_o (at $df/dI = 0$)	27 000, 90 000
Q_c (at $df/dI = 0$)	20 000, 15 000

90 MHz is observed from the 3.148 GHz resonator. Beyond the measured maximum frequency shift, both resonators exhibit a discontinuity where they snap back to their original (unbiased) resonant frequency and the frequency shift versus dc bias pattern repeats. Dashed lines show a fit to a polynomial relationship. Using Eq. (4) we calculate I^* to be 0.6 and 0.4 mA for resonators with 400 and 300 nm inductors, respectively. These values are larger than values estimated through the measured critical current I_c (52 and 39 μA) and the assumption that $I^* \approx I_c$. The internal quality factor, Q_o , of both resonators degrades with increasing current bias. For the 3.148 GHz resonator, Q_o changes from 90 000 to 20 000. For the 2.705 GHz resonator, Q_o changes from 27 000 to 15 000. Understanding this change in Q_o requires further study.

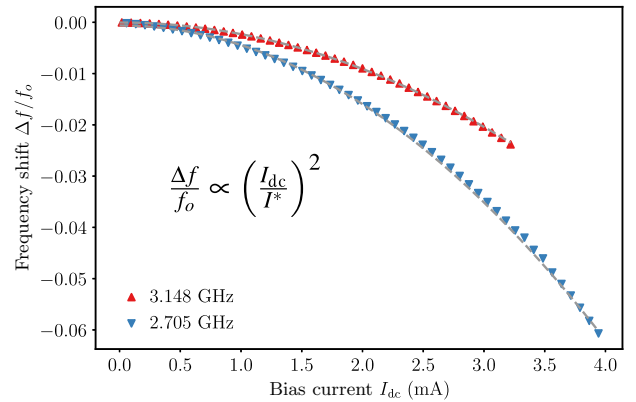


FIG. 3. Relative resonance shift $\Delta f/f_o$ as a function of dc bias current for the two aluminum resonators. The resonant frequency shifts to lower values with increasing biasing current following a parabolic relationship as expected from Eq. (4). Dashed lines are fits to a quadratic equation.

III. MIXING THROUGH FLUX BIASING

Our flux bias design also presents a mechanism for coupling ac signals. At lower frequencies, this attribute can be used to up-convert the signal. We can consider a low-frequency modulation at frequency ω_m with small-amplitude I_m superimposed on top of a dc bias for a total current on the readout line $I'_{\text{dc}} = I_{\text{dc}} + I_m \sin(\omega_m t)$. Using Eq. (A13) along with the first-order Taylor expansion $(I_{\text{dc}} + I_m \sin(\omega_m t))^2 \approx I_{\text{dc}}^2 + 2I_{\text{dc}}I_m \sin(\omega_m t)$ for $I_m \ll I_{\text{dc}}$, we can write the resonant frequency as

$$\omega'_o = \omega_o + \delta_{\text{dc}} + \delta_m, \quad (5)$$

where ω_o is the zero-bias resonant frequency, and

$$\delta_{\text{dc}} = -\frac{3\omega_o \alpha M^2 I_{\text{dc}}^2}{L_{\text{self}}^2 I^{*2}}, \quad (6)$$

$$\delta_m = -6 \frac{d\omega}{dI_{\text{dc}}} I_m \sin(\omega_m t), \quad (7)$$

correspond to the respective shifts in resonator frequency due to the dc bias and the modulation at ω_m . The response to the low-frequency modulation, δ_m , is a modulation which appears in frequency domain as sidebands at $\pm\omega_m$ on both sides of the resonator tone $\omega_o + \delta_{\text{dc}}$ with amplitude proportional to $d\omega/dI_{\text{dc}}$. We can demonstrate this up-conversion empirically by applying a 10-kHz modulation on the bias line with and without a dc bias. We observe a prominent appearance of ± 10 kHz sidebands around the resonator frequency with the application of a dc bias (see Fig. 4) while keeping all other measurement parameters the same.

Our flux coupling design can also be utilized for parametric pumping of signals near its resonant frequency through three-wave mixing [50,51]. The system Hamiltonian under three-wave mixing is given by

$$\begin{aligned} \mathcal{H} = & \hbar(\omega_o + \delta_{\text{dc}} + \delta_p + K - \frac{\omega_p}{2}) a^\dagger a \\ & + \frac{\hbar\xi}{2} a^{\dagger 2} + \frac{\hbar\xi^*}{2} a^2 + \frac{\hbar K}{2} a^{\dagger 2} a^2, \end{aligned} \quad (8)$$

with

$$\delta_p = -\frac{3\omega_o \alpha M^2 I_p^2}{4L_{\text{self}}^2 I^{*2}}, \quad (9)$$

$$K = -\frac{3\hbar\omega_o^2 \alpha}{2L_T I^{*2}}, \quad (10)$$

$$\xi = -\frac{3\omega_o \alpha M^2 I_{\text{dc}} I_p}{2L_{\text{self}}^2 I^{*2}} e^{-i\phi_p}. \quad (11)$$

where we have used Eq. (A9) to convert current in the loop (\bar{I}_{dc}) to bias current in the readout line (I_{dc}). Here ω_o is the

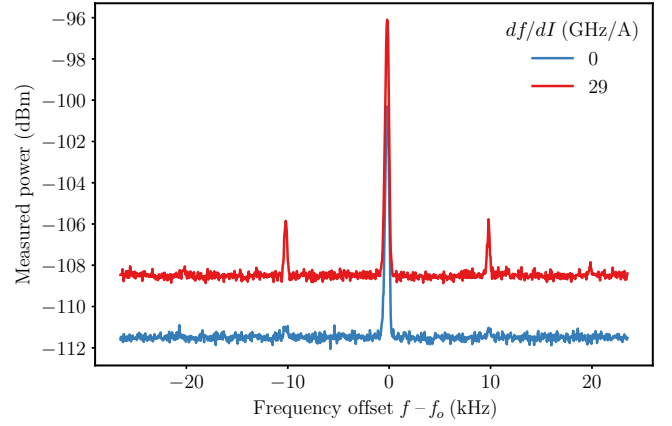


FIG. 4. Frequency up-conversion of a 10-kHz low-frequency signal through a carrier tone at resonator frequency $f_o = 3.148$ GHz. Without frequency detuning or current bias $df/dI_{\text{dc}} = 0$ minimum up-conversion is observed above the noise floor of our measurement (blue curve). Applying a dc bias that shifts the resonance by 10 MHz (corresponding to $df/dI_{\text{dc}} \neq 0$) we observe clear frequency up-conversion as sidebands around the center carrier peak (red curve).

zero-bias resonance frequency, L_T is the total inductance of the inductor which includes both geometric and kinetic inductance, δ_{dc} is same as in Eq. (6), δ_p is the resonance frequency shift from the pumping tone, K is the Kerr constant corresponding to the nonlinearity of the system, ξ is the mixing strength under three-wave mixing, and I_p is amplitude of the three-wave mixing tone ω_p (see Appendix C for detailed Hamiltonian construction).

We demonstrate the mixing process as follows: we apply a weak signal tone at frequency $\omega_s = \omega_o + \delta_{\text{dc}}$ and a strong pump tone at frequency $\omega_p = 2\omega_s + 8$ kHz to the readout line and measure the output signal with a spectrum analyzer. Three-wave mixing results in a signal at the idler frequency $\omega_i = \omega_s + 8$ kHz, which appears as a sideband at 8 kHz above the signal tone). Figure 5 shows the results from our measurements with the curves, from bottom up, corresponding to increasing pump power with all other parameters kept constant. The curves have been shifted vertically for clarity. The inset is an enlarged view at the idler tone showing that the power at the idler tone increases monotonically with the pump power, which is predicted by the dependence of the three-wave mixing rate ξ on the pump power I_p in Eq. (11).

We repeat this measurement by applying various dc biases which would also change the coupling strength. Results are shown in Fig. 6. From the system Hamiltonian, the strength of the three-wave mixing ξ increases linearly with dc current bias I_{dc} [Eq. (11)]. With each applied dc bias, we observe an expected shift in resonance frequency given by Eq. (9). We measured the idler sideband power for pump powers of -56 , -51 , and -46 dBm at three dc biases corresponding to frequency detunings of $(0, -5,$

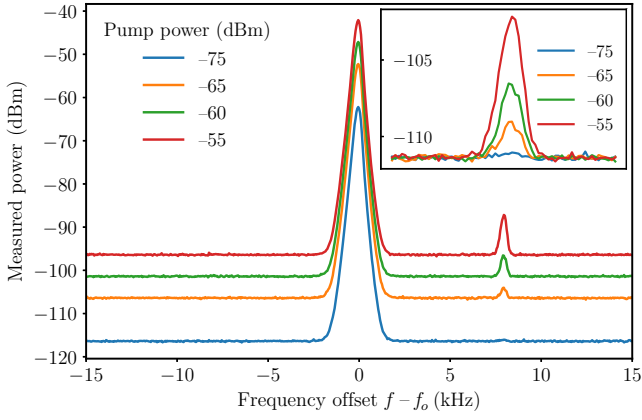


FIG. 5. Measured three-wave mixing power spectrum for resonator with resonant frequency $f_o = 3.145$ GHz. From bottom to top, the curves correspond to monotonically increasing pump power. The curves are shifted vertically for better idler tone visibility. Pump power is calculated by subtracting the total loss in the input line from the output power of the signal generator. Both pump and signal generators as well spectrum analyzer are frequency locked through 10-MHz reference ports. The inset is an enlarged view of the idler tone without vertical shift. The horizontal axis is frequency and the vertical axis is power in dBm. Legend is pump power in dBm. For pump power from -75 to -55 dBm the idler power increases from close to zero to 10 dB relative to the noise floor on the spectrum analyzer.

and -10 MHz). At each detuning we linearly fit the sideband power to its pump power and observe that the slope of the fitted lines increases monotonically with detuning magnitude, which is consistent with the predicted increase in coupling strength.

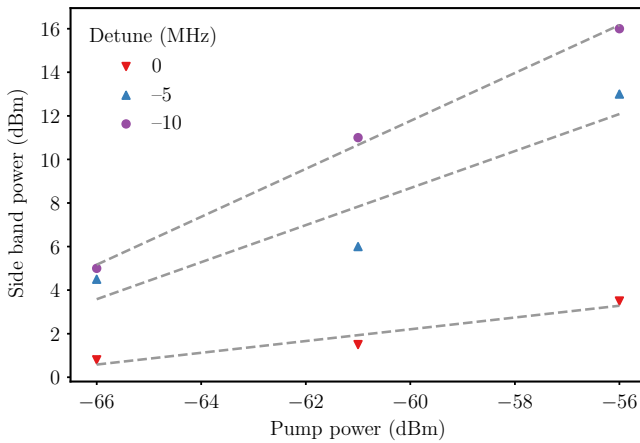


FIG. 6. Sideband power as function of pump power for three different frequency detuning or current bias points. In this power measurement we have deducted the noise floor of the spectrum analyzer from the peak power of the sidebands.

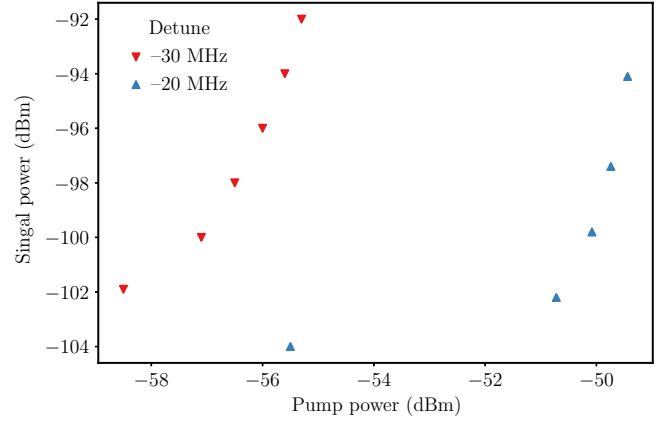


FIG. 7. Measured signal peak power under nondegenerate three-wave pumping as function of pump power at two frequency detuning points.

IV. DISCUSSION

Motivated by the three-wave mixing result, we also qualitatively investigated the potential of the flux bias resonator to be used as a parametric amplifier. First, we operated the amplifier with nondegenerate three-wave pumping where the signal with power of -130 dBm is detuned 4 kHz above resonant frequency and the pump is set at twice the resonant frequency. The signal peak power is measured with a spectrum analyzer. Figure 7 shows the measured signal power as a function of pump power at two dc biases corresponding to two frequency detunings. The increased dc flux bias results in both larger detuning and a boost of the three-wave mixing strength ξ . Increasing the pump power eventually results in 10 dB gain on the signal for both detunings with the larger detuning showing amplification at lower pump amplitudes. This corresponds with the theoretical prediction that ξ is linearly proportional to both I_{dc} in the resonator as well as the pumping current amplitude I_p . At signal power about -100 dBm amplification gain saturates and signal peak stops responding to pump power change. If compared with JJ and high-kinetic-inductance material-based parametric amplifiers with gain ranging from 10 to 40 dB [35,51–53], the 10-dB gain from our nonlinear resonator is limited by its lower kinetic inductance of the aluminum film. Larger gain is expected when using materials with a high kinetic inductance.

We also characterized the device gain under degenerate three-wave mixing, when a signal tone at the resonator frequency with power of -130 dBm and a pump tone at twice the resonator frequency are applied. Under this condition the pump signal splits into pairs of signal and idler photons that are of the same frequency and the system gain varies with the phase difference between the pump and the signal. Results of the measured signal peak as a function of the pump tone phase are shown in Fig. 8. Since the signal phase remains constant, changing the pump phase

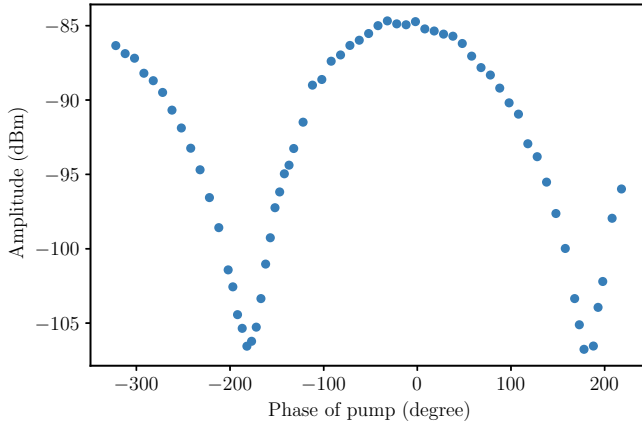


FIG. 8. Measured signal peak power under degenerate three-wave pumping as a function of pump phase. Both signal power and phase as well as pump output power from generator remain constant during measurement while phase of the pump was changed by adjusting the phase parameter on the generator. The power of the pump was set at -51 dBm. An arbitrary phase offset has been removed to set the phase maximum at zero.

changes the relative phase between the pump and the signal and the measurement clearly demonstrates dependence of the amplification on the pump phase with a period of 2π . On the other hand, we varied the phase of the signal while keeping the pump phase constant and observed the expected change in amplification modulation period from 2π to π .

As with other resonance-based parametric amplifiers, the gain bandwidth of our design (~ 100 kHz) is determined by the resonance quality factor. Since the resonance can be tuned over 100 MHz range by adjusting dc current bias the amplification can cover an effective working bandwidth of 100 MHz. This is similar to other tunable or impedance-matched parametric amplifiers [35,54].

V. CONCLUSION

In conclusion, we have demonstrated the flux-bias tuning of the resonant frequency of a superconducting resonator by using the screening current induced by magnetic flux through a superconducting loop in combination with the nonlinear inductance of a superconducting thin film. Our devices exhibit the expected frequency detuning as demonstrated by measurements of the frequency response for varying dc flux bias, along with the mixing of low-frequency (\sim MHz) and high-frequency (\sim GHz) signals. Our measurements also provides an initial demonstration of potential applications of this architecture including up-converting megahertz signals and parametric amplification through three-wave mixing. Larger frequency detuning can potentially be achieved by fabricating devices with narrower and thinner loop wires and using other superconducting films such as titanium nitride [55] or niobium

nitride [56], NbTi [57], YBCO [58,59], and granular aluminum [60,61], which have very high kinetic inductance and, hence, larger ratio of kinetic to geometric inductance. Consequently, the resonator size will be reduced if the same resonant frequency is to be maintained. This adjustment in resonator size has insignificant impact on frequency tunability, because both the external flux threading the loop (Φ_{dc}) and the self-inductance of the loop (L_{self}) decrease. Furthermore, devices using alternative materials with higher critical temperature may also enable operation at temperatures above 4 K.

Data used in this work is available on reasonable request.

ACKNOWLEDGMENTS

We thank Professor Jarryd Pla from UNSW of Sydney, Australia for very helpful discussion on system Hamiltonian construction. Work at Argonne National Laboratory, including work performed at the Center for Nanoscale Materials, a US Department of Energy Office of Science User Facility, is supported by the US Department of Energy, Office of Science, Office of High Energy Physics and Office of Basic Energy Sciences, under Contract No. DE-AC02-06CH11357. This material is based upon work supported by the US Department of Energy Office of Science National Quantum Information Science Research Centers. The work at *Q*-Next includes concept development, design, fabrication, testing, and modeling of devices.

APPENDIX A: CALCULATION OF $df/d\Phi$

Complete solution for self-inductance of a rectangular loop is given as [62]

$$L_{self} = \frac{\mu_0 \mu_r}{\pi} \left[-2(w+h) + 2\sqrt{h^2 + w^2} + \text{temp} \right], \quad (\text{A1})$$

with

$$\begin{aligned} \text{temp} = & -h \ln \left(\frac{h + \sqrt{h^2 + w^2}}{w} \right) - w \ln \left(\frac{w + \sqrt{h^2 + w^2}}{h} \right) \\ & + h \ln \left(\frac{2h}{d/2} \right) + w \ln \left(\frac{2w}{d/2} \right), \end{aligned}$$

where w and h are the width and height of the inductor square loop, and d is the diameter of the inductor wire. We ignore the small correction to this expression due to the presence of a ground plane [63].

TABLE II. Mathematical symbols and corresponding definition.

Symbol	Definition
ω_o	Angular frequency of flux biased resonator
ω_m	Angular frequency of modulation tone
L_k	Kinetic inductance of Al inductor
$L_{k,o}$	Intrinsic kinetic inductance of Al inductor
I_{sc}	Screening current of superconducting loop
I^*	Characteristic current of Al inductor
L_{self}	Self-inductance of superconducting loop
Φ_{dc}	External flux threading the superconducting loop
Φ_o	Flux quantum
I_{dc}	dc bias current in the readout line
\bar{I}_{dc}	dc current in superconducting loop
\bar{I}_p	Pump current in superconducting loop
L_o	Geometric inductance of inductor
L_T	Total inductance of inductor
α	Kinetic inductance participation ratio
M	Mutual inductance between readout line and loop
K	Kerr nonlinearity of the flux biased resonator
Q_o	Internal quality factor
Q_c	External of coupling quality factor

The resonant frequency of an LC resonator is given by

$$f_t = \frac{1}{2\pi\sqrt{L_t C_t}} = \frac{1}{2\pi\sqrt{(L_o + L_{k,o} + \Delta L_k) C_t}} \quad (A2)$$

$$= \frac{1}{2\pi\sqrt{(L_o + L_{k,o}) C_t}} \left(1 - \frac{\Delta L_k}{2(L_o + L_{k,o})}\right) \quad (A3)$$

$$= f_o \left(1 - \frac{\Delta L_k}{2(L_o + L_{k,o})}\right), \quad (A4)$$

with $f_o = 1/(2\pi\sqrt{(L_o + L_{k,o}) C_t})$ and $\Delta L_k = L_{k,o} (I_{sc}/I^*)^2$

The relative frequency shift due to change in kinetic inductance is expressed as

$$\frac{\Delta f}{f_o} = \frac{f - f_o}{f_o} = \frac{-\Delta L_k}{2(L_o + L_{k,o})} \quad (A5)$$

$$= \frac{L_{k,o}}{2(L_o + L_{k,o})} \left(\frac{I_{sc}}{I^*}\right)^2 \quad (A6)$$

$$= \frac{L_{k,o}}{2(L_o + L_{k,o})} \left(\frac{I_{sc}}{I^*}\right)^2. \quad (A7)$$

Expressing the screening current I_{sc} from Eq. (2)

$$I_{sc} = \frac{-\Phi_{dc} + m\Phi_o}{L_{self}} \quad (A8)$$

$$= \frac{-MI_{dc} + m\Phi_o}{L_{self}}, \quad (A9)$$

where M is the mutual inductance between the readout line and the superconducting loop. Substituting I_{sc} into Eq.

(A9) we obtain

$$\frac{\Delta f}{f_o} = \frac{L_{k,o}}{2L_{self}} \left(\frac{I_{sc}}{I^*}\right)^2 \quad (A10)$$

$$= \frac{L_{k,o}(-MI_{dc} + m\Phi_o)^2}{2(L_o + L_{k,o})L_{self}^2 I^{*2}} \quad (A11)$$

$$= \frac{\alpha(-MI_{dc} + m\Phi_o)^2}{2L_{self}^2 I^{*2}}. \quad (A12)$$

The derivative of frequency change versus current bias is

$$\frac{df}{dI_{dc}} = \frac{f_o \alpha M^2}{L_{self}^2 I^{*2}} I_{dc}, \quad (A13)$$

where we have set the intrinsic loop flux $m = 0$.

APPENDIX B: OPTIMIZATION OF $df/d\Phi$

Several geometrical factors play role in determining the relative magnitude of resonance frequency shift induced by the I_{dc} : the resonator geometry such as the width and length of the loop and the cross-section of the superconducting microstrip, as well as the mutual inductance between the resonator loop and the dc line. In our resonator design $Q_c \ll Q_o$ so the total quality factor Q_r is dominated by Q_c . We choose the width of the loop to be 500 μm because it gives us the high Q_c based on our related resonator design. It will be easier to achieve flux bias with a wider loop but at the same time Q_c will decrease. The gap between the resonator and the readout line is 2 μm . A smaller gap will have more flux bias but it would also bring challenges related to lithographic patterning of the structure. At this point we prefer to limit ourself with the best resolution of our optical lithography. Thus, in our designs we fixed the width to be 500 μm and gap to be 2 μm .

In Fig. 9 we plot the df/dI_{dc} as function of the loop height H from 0 to 10 000 μm for loop microstrip width of 1 μm and the maximum frequency shift happens at $H \approx 200 \mu\text{m}$. This gives a guideline regarding the target parameters of the resonator design.

APPENDIX C: NONLINEAR RESONATOR MODEL

For a kinetic-inductance-based nonlinear resonator

$$L_k(I) = L_{k,o} \left(1 + \frac{I^2}{I^{*2}}\right), \quad (C1)$$

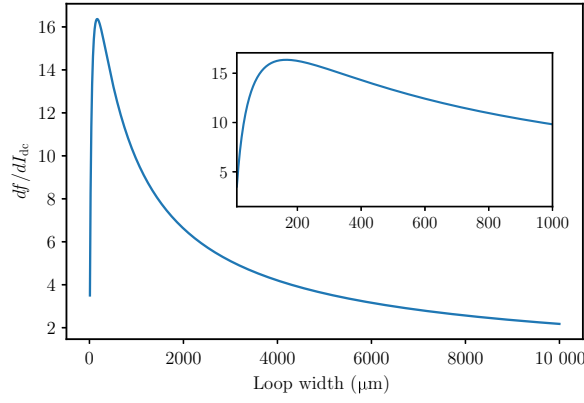


FIG. 9. Plot of $\partial f / \partial I_{dc}$ as a function of loop width W for loop strip of $1 \mu\text{m}$. Maximum happens at $W \approx 200 \mu\text{m}$. The inset is an enlarged view of the range of $1000 \mu\text{m}$ to show the maximum point.

the calculated energy of the resonator is as follows:

$$U_C = \frac{1}{2} C \Phi^2, \quad (\text{C2})$$

$$U_L = \frac{1}{2} \frac{\Phi^2}{L_k + L_o} \quad (\text{C3})$$

$$= \frac{1}{2} \frac{\Phi^2}{L_{o,k} \left(1 + \frac{L^2}{I^{*2}}\right) + L_o} \quad (\text{C4})$$

$$= \frac{1}{2} \frac{\Phi^2}{L_T} - \frac{L_{o,k}}{2L_T^4 I^{*2}} \Phi^4, \quad (\text{C5})$$

where $L_T = L_o + L_{k,o}$. Here L_o and $L_{k,o}$ are the geometric and kinetic inductance without current bias, respectively. The Lagrangian of the resonator is given as

$$\mathcal{L} = U_C - U_L = \frac{1}{2} C \dot{\Phi}^2 - \frac{1}{2} \frac{\Phi^2}{L_T} + \frac{L_{o,k}}{2L_T^4 I^{*2}} \Phi^4. \quad (\text{C6})$$

Using Legendre transformation $\mathcal{H} = \dot{\Phi} Q - \mathcal{L}$ the Hamiltonian is written as follows:

$$\mathcal{H} = \frac{Q^2}{2C} + \frac{1}{2} \frac{\Phi^2}{L_T} - \frac{L_{o,k}}{2L_T^4 I^{*2}} \Phi^4. \quad (\text{C7})$$

Replacing Q and Φ with their quantum operators \hat{Q} and $\hat{\Phi}$, the Hamiltonian can now be written as

$$\tilde{\mathcal{H}} = \frac{\tilde{Q}^2}{2C} + \frac{1}{2} \frac{\tilde{\Phi}^2}{L_T} - \frac{L_{o,k}}{2L_T^4 I^{*2}} \tilde{\Phi}^4, \quad (\text{C8})$$

we can further separate the Hamiltonian into its linear $\tilde{\mathcal{H}}_o$ and interaction $\tilde{\mathcal{H}}_I$ part

$$\tilde{\mathcal{H}}_o = \frac{\tilde{Q}^2}{2C} + \frac{1}{2} \frac{\tilde{\Phi}^2}{L_T}, \quad (\text{C9})$$

$$\tilde{\mathcal{H}}_I = -\frac{L_{o,k}}{2L_T^4 I^{*2}} \tilde{\Phi}^4. \quad (\text{C10})$$

Defining the following creation and annihilation operators with $\omega_o = 1/\sqrt{L_T C}$:

$$\tilde{a} = \frac{1}{\sqrt{\hbar\omega_o}} \left[\frac{1}{\sqrt{2L_T}} \tilde{\Phi} + i \frac{1}{\sqrt{2C}} \tilde{Q} \right], \quad (\text{C11})$$

$$\tilde{a}^\dagger = \frac{1}{\sqrt{\hbar\omega_o}} \left[\frac{1}{\sqrt{2L_T}} \tilde{\Phi} - i \frac{1}{\sqrt{2C}} \tilde{Q} \right], \quad (\text{C12})$$

the reduced flux operator in terms of \tilde{a} and \tilde{a}^\dagger

$$\tilde{\Phi} = \sqrt{\hbar\omega_o L_T / 2} (\tilde{a}^\dagger + \tilde{a}), \quad (\text{C13})$$

and the interaction Hamiltonian is

$$\mathcal{H}_I = -\frac{L_{o,k}}{2L_T^4 I^{*2}} (\hbar\omega_o L_T / 2)^2 (\tilde{a}^\dagger + \tilde{a})^4 \quad (\text{C14})$$

$$= -\frac{3L_{o,k} (\hbar\omega_o L_T)^2}{4L_T^4 I^{*2}} (2\tilde{a}^\dagger \tilde{a} + \tilde{a}^{\dagger 2} \tilde{a}^2) \quad (\text{C15})$$

$$= \hbar K \tilde{a}^\dagger \tilde{a} + \frac{1}{2} \hbar K \tilde{a}^{\dagger 2} \tilde{a}^2, \quad (\text{C16})$$

and $K = -3\hbar\omega_o^2 L_{o,k} / 2L_T^2 I^{*2} = -3\hbar\omega_o^2 \alpha / 2L_T I^{*2}$. Here α is the participation ratio of the kinetic inductance with dc bias \bar{I}_{dc} and parametric pump mode \bar{I}_p in the resonator

$$\begin{aligned} \mathcal{H}_I &= \frac{1}{2} \hbar K \left(2a^\dagger a + a^{\dagger 2} a^2 \right) - \frac{L_{o,k}}{2L_T^4 I^{*2}} 6(\hbar\omega_o L_T / 2) L_T^2 \\ &\quad \times \left[\bar{I}_{dc}^2 + 2\bar{I}_{dc} \bar{I}_p(t) + \bar{I}_p^2(t) \right] \left(2a^\dagger a + a^{\dagger 2} + a^2 \right) \end{aligned} \quad (\text{C17})$$

$$\begin{aligned} &= \frac{1}{2} \hbar K \left(2a^\dagger a + a^{\dagger 2} a^2 \right) - \frac{3\hbar\omega_o \alpha}{2I^{*2}} \\ &\quad \times \left[\bar{I}_{dc}^2 + 2\bar{I}_{dc} \bar{I}_p(t) + \bar{I}_p^2(t) \right] \left(2a^\dagger a + a^{\dagger 2} + a^2 \right), \end{aligned} \quad (\text{C18})$$

the time-dependent pump mode can be written as

$$\bar{I}_p(t) = \frac{\bar{I}_p}{2} \left(e^{-i(\omega_p t + \phi_p)} + e^{i(\omega_p t + \phi_p)} \right). \quad (\text{C19})$$

Next we apply rotating wave approximation (RWA)

$$\mathcal{H}'_I = U^\dagger \mathcal{H}_I U - i\hbar U^\dagger \frac{\partial}{\partial t} U \quad (\text{C20})$$

and

$$U^\dagger = \exp(i\omega_p t a^\dagger a/2) \quad (\text{C21})$$

$$U = \exp(-i\omega_p t a^\dagger a/2). \quad (\text{C22})$$

We transfer the Hamiltonian into frame rotating at $\omega_p/2$

$$\mathcal{H} = \hbar(\omega_o + \delta_{\text{dc}} + \delta_p + K - \frac{\omega_p}{2})a^\dagger a \quad (\text{C23})$$

$$+ \frac{\hbar\xi}{2}a^{\dagger 2} + \frac{\hbar\xi^*}{2}a^2 + \frac{\hbar K}{2}a^{\dagger 2}a^2, \quad (\text{C24})$$

$$\delta_{\text{dc}} = -\frac{3\omega_o\alpha\bar{I}_{\text{dc}}^2}{I^{*2}}, \quad (\text{C25})$$

$$\delta_p = -\frac{3\omega_o\alpha\bar{I}_p^2}{4I^{*2}}, \quad (\text{C26})$$

$$K = -\frac{3\hbar\omega_o^2\alpha}{2L_T I^{*2}}, \quad (\text{C27})$$

$$\xi = -\frac{3\omega_o\alpha\bar{I}_{\text{dc}}\bar{I}_p}{2I^{*2}}e^{-i\phi_p}, \quad (\text{C28})$$

the system Hamiltonian can be calculated by setting the pump amplitude to zero and

$$\mathcal{H} = \hbar(\omega_o + \delta_{\text{dc}} + K)a^\dagger a + \frac{\hbar K}{2}a^{\dagger 2}a^2, \quad (\text{C29})$$

$$\delta_{\text{dc}} = -\frac{3\omega_o\alpha\bar{I}_{\text{dc}}^2}{I^{*2}}. \quad (\text{C30})$$

-
- [1] P. K. Day, H. G. LeDuc, B. A. Mazin, A. Vayonakis, and J. Zmuidzinas, A broadband superconducting detector suitable for use in large arrays, *Nature* **425**, 817 (2003).
- [2] N. Crescini, D. Alesini, C. Braggio, G. Carugno, D. D'Agostino, D. Di Gioacchino, P. Falferi, U. Gambardella, C. Gatti, G. Iannone, C. Ligi, A. Lombardi, A. Ortolan, R. Pengo, G. Ruoso, and L. Taffarello, (QUAX Collaboration), Axion search with a quantum-limited ferromagnetic haloscope, *Phys. Rev. Lett.* **124**, 171801 (2020).
- [3] R. Di Vora, *et al.*, (QUAX Collaboration), Search for galactic axions with a traveling wave parametric amplifier, *Phys. Rev. D* **108**, 062005 (2023).
- [4] A. Blank, Y. Twig, and Y. Ishay, Recent trends in high spin sensitivity magnetic resonance, *J. Magn. Reson.* **280**, 20 (2017)., Special issue on Methodological advances in EPR spectroscopy and imaging
- [5] N. Abhyankar, A. Agrawal, J. Campbell, T. Maly, P. Shrestha, and V. Szalai, Recent advances in microresonators and supporting instrumentation for electron paramagnetic resonance spectroscopy, *Rev. Sci. Instrum.* **93**, 101101 (2022).

- [6] A. Wallraff, D. I. Schuster, A. Blais, L. Frunzio, R.-S. Huang, J. Majer, S. Kumar, S. M. Girvin, and R. J. Schoelkopf, Strong coupling of a single photon to a superconducting qubit using circuit quantum electrodynamics, *Nature* **431**, 162 (2004).
- [7] A. Blais, R.-S. Huang, A. Wallraff, S. M. Girvin, and R. J. Schoelkopf, Cavity quantum electrodynamics for superconducting electrical circuits: An architecture for quantum computation, *Phys. Rev. A* **69**, 062320 (2004).
- [8] Y. Kubo, C. Grezes, A. Dewes, T. Umeda, J. Isoya, H. Sumiya, N. Morishita, H. Abe, S. Onoda, T. Ohshima, V. Jacques, A. Dréau, J.-F. Roch, I. Diniz, A. Auffèves, D. Vion, D. Esteve, and P. Bertet, Hybrid quantum circuit with a superconducting qubit coupled to a spin ensemble, *Phys. Rev. Lett.* **107**, 220501 (2011).
- [9] J. D. Teufel, D. Li, M. S. Allman, K. Cicak, A. J. Sirois, J. D. Whittaker, and R. W. Simmonds, Circuit cavity electromechanics in the strong-coupling regime, *Nature* **471**, 204 (2011).
- [10] X. Han, C.-L. Zou, and H. X. Tang, Multimode strong coupling in superconducting cavity piezoelectromechanics, *Phys. Rev. Lett.* **117**, 123603 (2016).
- [11] J. Bochmann, A. Vainsencher, D. D. Awschalom, and A. N. Cleland, Nanomechanical coupling between microwave and optical photons, *Nat. Phys.* **9**, 712 (2013).
- [12] K. C. Balram, M. I. Davanço, J. D. Song, and K. Srinivasan, Coherent coupling between radiofrequency, optical and acoustic waves in piezo-optomechanical circuits, *Nat. Photonics* **10**, 346 (2016).
- [13] S. Barzanjeh, M. Abdi, G. J. Milburn, P. Tombesi, and D. Vitali, Reversible optical-to-microwave quantum interface, *Phys. Rev. Lett.* **109**, 130503 (2012).
- [14] R. W. Andrews, R. W. Peterson, T. P. Purdy, K. Cicak, R. W. Simmonds, C. A. Regal, and K. W. Lehnert, Bidirectional and efficient conversion between microwave and optical light, *Nat. Phys.* **10**, 321 (2014).
- [15] B. Brock, J. Li, S. Kanhirathingal, B. Thyagarajan, M. Blencowe, and A. Rimberg, Fast and ultrasensitive electrometer operating at the single-photon level, *Phys. Rev. Appl.* **16**, L051004 (2021).
- [16] C. E. Bradley, J. Randall, M. H. Abobeih, R. C. Berrevoets, M. J. Degen, M. A. Bakker, M. Markham, D. J. Twitchen, and T. H. Taminiau, A ten-qubit solid-state spin register with quantum memory up to one minute, *Phys. Rev. X* **9**, 031045 (2019).
- [17] S. Kitazawa, Y. Matsuzaki, S. Saijo, K. Kakuyanagi, S. Saito, and J. Ishi-Hayase, Vector-magnetic-field sensing via multifrequency control of nitrogen-vacancy centers in diamond, *Phys. Rev. A* **96**, 042115 (2017).
- [18] A. A. Fursina and A. Sinitskii, Toward molecular spin qubit devices: Integration of magnetic molecules into solid-state devices, *ACS Appl. Electron. Mater.* **5**, 3531 (2023).
- [19] A. G. Claudio Bonizzoni and M. Affronte, Coherent coupling of molecular spins with microwave photons in planar superconducting resonators, *Adv. Phys. X* **3**, 1435305 (2018).
- [20] I. Gimeno, A. Urtizbera, J. Román-Roche, D. Zueco, A. Camón, P. J. Alonso, O. Roubeau, and F. Luis, Broad-band spectroscopy of a vanadyl porphyrin: A model electronuclear spin qubit, *Chem. Sci.* **12**, 5621 (2021).

- [21] X. Zhang, C.-L. Zou, N. Zhu, F. Marquardt, L. Jiang, and H. X. Tang, Magnon dark modes and gradient memory, *Nat. Commun.* **6**, 8914 (2015).
- [22] D. Lachance-Quirion, Y. Tabuchi, A. Gloppe, K. Usami, and Y. Nakamura, Hybrid quantum systems based on magnonics, *Appl. Phys. Express* **12**, 070101 (2019).
- [23] I. A. Golovchanskiy, N. N. Abramov, V. S. Stolyarov, M. Weides, V. V. Ryazanov, A. A. Golubov, A. V. Ustinov, and M. Y. Kupriyanov, Ultrastrong photon-to-magnon coupling in multilayered heterostructures involving superconducting coherence via ferromagnetic layers, *Science Advances* **7**, eabe8638 (2021).
- [24] A. Ghirri, C. Bonizzoni, M. Maksutoglu, A. Mercurio, O. Di Stefano, S. Savasta, and M. Affronte, Ultrastrong magnon-photon coupling achieved by magnetic films in contact with superconducting resonators, *Phys. Rev. Appl.* **20**, 024039 (2023).
- [25] C. L. Degen, F. Reinhard, and P. Cappellaro, Quantum sensing, *Rev. Mod. Phys.* **89**, 035002 (2017).
- [26] K. Yahata, Y. Matsuzaki, S. Saito, H. Watanabe, and J. Ishi-Hayase, Demonstration of vector magnetic field sensing by simultaneous control of nitrogen-vacancy centers in diamond using multi-frequency microwave pulses, *Appl. Phys. Lett.* **114**, 022404 (2019).
- [27] J. Meinel, V. Vorobyov, B. Yavkin, D. Dasari, H. Sumiya, S. Onoda, J. Isoya, and J. Wrachtrup, Heterodyne sensing of microwaves with a quantum sensor, *Nat. Commun.* **12**, 2737 (2021).
- [28] C. Bonizzoni, A. Ghirri, F. Santanni, and M. Affronte, Quantum sensing of magnetic fields with molecular spins, *npj Quantum Inf.* **10**, 41 (2024).
- [29] S. P. Wolski, D. Lachance-Quirion, Y. Tabuchi, S. Kono, A. Noguchi, K. Usami, and Y. Nakamura, Dissipation-based quantum sensing of magnons with a superconducting qubit, *Phys. Rev. Lett.* **125**, 117701 (2020).
- [30] D. Lachance-Quirion, Y. Tabuchi, S. Ishino, A. Noguchi, T. Ishikawa, R. Yamazaki, and Y. Nakamura, Resolving quanta of collective spin excitations in a millimeter-sized ferromagnet, *Sci. Adv.* **3**, e1603150 (2017).
- [31] D. Das, A. Naji, K. K. S. Multani, A. H. Safavi-Naeini, and E. A. Nanni, in *2022 47th International Conference on Infrared, Millimeter and Terahertz Waves (IRMMW-THz) (IEEE, 2022)*, p. 1.
- [32] M. Sandberg, C. M. Wilson, F. Persson, T. Bauch, G. Johansson, V. Shumeiko, T. Duty, and P. Delsing, Tuning the field in a microwave resonator faster than the photon lifetime, *Appl. Phys. Lett.* **92**, 203501 (2008).
- [33] Z. L. Wang, Y. P. Zhong, L. J. He, H. Wang, J. M. Martinis, A. N. Cleland, and Q. W. Xie, Quantum state characterization of a fast tunable superconducting resonator, *Appl. Phys. Lett.* **102**, 163503 (2013).
- [34] B. Abdo, A. Kamal, and M. Devoret, Nondegenerate three-wave mixing with the Josephson ring modulator, *Phys. Rev. B* **87**, 014508 (2013).
- [35] M. A. Castellanos-Beltran and K. W. Lehnert, Widely tunable parametric amplifier based on a superconducting quantum interference device array resonator, *Appl. Phys. Lett.* **91**, 083509 (2007).
- [36] K. D. Osborn, J. A. Strong, A. J. Sirois, and R. W. Simmonds, Frequency-tunable Josephson junction resonator for quantum computing, *IEEE Trans. Appl. Supercond.* **17**, 166 (2007).
- [37] A. Palacios-Laloy, F. Nguyen, F. Mallet, P. Bertet, D. Vion, and D. Esteve, Tunable resonators for quantum circuits, *J. Low Temp. Phys.* **151**, 1034 (2008).
- [38] O. Kennedy, J. Burnett, J. Fenton, N. Constantino, P. Warburton, J. Morton, and E. Dupont-Ferrier, Tunable Nb superconducting resonator based on a constriction nanosquid fabricated with a Ne focused ion beam, *Phys. Rev. Appl.* **11**, 014006 (2019).
- [39] C. W. Zollitsch, J. O'Sullivan, O. Kennedy, G. Dold, and J. J. L. Morton, Tuning high- Q superconducting resonators by magnetic field reorientation, *AIP Advances* **9**, 125225 (2019).
- [40] M. Xu, X. Han, W. Fu, C.-L. Zou, and H. X. Tang, Frequency-tunable high- Q superconducting resonators via wireless control of nonlinear kinetic inductance, *Appl. Phys. Lett.* **114**, 192601 (2019).
- [41] J. E. Healey, T. Lindström, M. S. Colclough, C. M. Muirhead, and A. Y. Tzalenchuk, Magnetic field tuning of coplanar waveguide resonators, *Appl. Phys. Lett.* **93**, 043513 (2008).
- [42] M. R. Vissers, J. Hubmayr, M. Sandberg, S. Chaudhuri, C. Bockstiegel, and J. Gao, Frequency-tunable superconducting resonators via nonlinear kinetic inductance, *Appl. Phys. Lett.* **107**, 062601 (2015).
- [43] N. Samkharadze, A. Bruno, P. Scarlino, G. Zheng, D. P. DiVincenzo, L. DiCarlo, and L. M. K. Vandersypen, High-kinetic-inductance superconducting nanowire resonators for circuit QED in a magnetic field, *Phys. Rev. Appl.* **5**, 044004 (2016).
- [44] A. Kher, P. K. Day, B. H. Eom, J. Zmuidzinas, and H. G. Leduc, Kinetic inductance parametric up-converter, *J. Low Temp. Phys.* **184**, 480 (2016).
- [45] A. A. Adamyan, S. E. Kubatkin, and A. V. Danilov, Tunable superconducting microstrip resonators, *Appl. Phys. Lett.* **108**, 172601 (2016).
- [46] J. Luomahaara, V. Vesterinen, L. Grönberg, and J. Hassel, Kinetic inductance magnetometer, *Nat. Commun.* **5**, 4872 (2014).
- [47] S. Mahashabde, E. Otto, D. Montemurro, S. de Graaf, S. Kubatkin, and A. Danilov, Fast tunable high- Q -factor superconducting microwave resonators, *Phys. Rev. Appl.* **14**, 044040 (2020).
- [48] S. Anlage, H. Snortland, and M. Beasley, A current controlled variable delay superconducting transmission line, *IEEE Trans. Magn.* **25**, 1388 (1989).
- [49] A. J. Annunziata, Single-Photon Detection, Kinetic Inductance, and Non-Equilibrium Dynamics in Niobium and Niobium Nitride Superconducting Nanowires, Ph.D. thesis, Yale University, Connecticut (2010).
- [50] C. Macklin, K. O'Brien, D. Hover, M. E. Schwartz, V. Bolkhovskoy, X. Zhang, W. D. Oliver, and I. Siddiqi, A near-quantum-limited Josephson traveling-wave parametric amplifier, *Science* **350**, 307 (2015).
- [51] D. J. Parker, M. Savytskyi, W. Vine, A. Laucht, T. Duty, A. Morello, A. L. Grimsmo, and J. J. Pla, Degenerate parametric amplification via three-wave mixing using kinetic inductance, *Phys. Rev. Appl.* **17**, 034064 (2022).

- [52] B. Yurke, L. R. Corruccini, P. G. Kaminsky, L. W. Rupp, A. D. Smith, A. H. Silver, R. W. Simon, and E. A. Whittaker, Observation of parametric amplification and deamplification in a Josephson parametric amplifier, *Phys. Rev. A* **39**, 2519 (1989).
- [53] N. Bergeal, F. Schackert, M. Metcalfe, R. Vijay, V. E. Manucharyan, L. Frunzio, D. E. Prober, R. J. Schoelkopf, S. M. Girvin, and M. H. Devoret, Phase-preserving amplification near the quantum limit with a Josephson ring modulator, *Nature* **465**, 64 (2010).
- [54] J. Grebel, A. Bienfait, E. Dumur, H.-S. Chang, M.-H. Chou, C. R. Conner, G. A. Peairs, R. G. Povey, Y. P. Zhong, and A. N. Cleland, Flux-pumped impedance-engineered broadband Josephson parametric amplifier, *Appl. Phys. Lett.* **118**, 142601 (2021).
- [55] J. Longden, F. Boussaha, C. Chaumont, K. Ratter, and B.-K. Tan, in *Quantum Technology: Driving Commercialisation of an Enabling Science II*, edited by M. J. Padgett, K. Bongs, A. Fedrizzi, and A. Politi, International Society for Optics and Photonics (SPIE, Glasgow, UK, 2021), Vol. 11881, p. 1188113.
- [56] S. Frasca, I. Arabadzhev, S. B. de Puechredon, F. Oppliger, V. Jouanny, R. Musio, M. Scigliuzzo, F. Minganti, P. Scarlino, and E. Charbon, Nbn films with high kinetic inductance for high-quality compact superconducting resonators, *Phys. Rev. Appl.* **20**, 044021 (2023).
- [57] R. Russo, A. Chatel, N. Şahin Solmaz, R. Farsi, H. Furci, J. Brugger, and G. Boero, Fabrication and characterization of NbTi microwave superconducting resonators, *Micro Nano Eng.* **19**, 100203 (2023).
- [58] A. Ghirri, C. Bonizzoni, D. Gerace, S. Sanna, A. Cassinese, and M. Affronte, YBa₂Cu₃O₇ microwave resonators for strong collective coupling with spin ensembles, *Appl. Phys. Lett.* **106**, 184101 (2015).
- [59] Z. Velluire-Pellat, E. Maréchal, N. Moulouguet, G. Saïz, G. C. Ménard, S. Kozlov, F. Couëdo, P. Amari, C. Medous, J. Paris, R. Hostein, J. Lesueur, C. Feuillet-Palma, and N. Bergeal, Hybrid quantum systems with high- T_c superconducting resonators, *Sci. Rep.* **13**, 14366 (2023).
- [60] L. Grünhaupt, M. Spiecker, D. Gusenkova, N. Maleeva, S. T. Skacel, I. Takmakov, F. Valenti, P. Winkel, H. Rotzinger, W. Wernsdorfer, A. V. Ustinov, and I. M. Pop, Granular aluminium as a superconducting material for high-impedance quantum circuits, *Nat. Mater.* **18**, 816 (2019).
- [61] N. Maleeva, L. Grünhaupt, T. Klein, F. Levy-Bertrand, O. Dupre, M. Calvo, F. Valenti, P. Winkel, F. Friedrich, W. Wernsdorfer, A. V. Ustinov, H. Rotzinger, A. Monfaradini, M. V. Fistul, and I. M. Pop, Circuit quantum electrodynamics of granular aluminum resonators, *Nat. Commun.* **9**, 3889 (2018).
- [62] C. R. Paul, *Inductance: Loop and Partial* (Wiley-IEEE Press, 2009).
- [63] X. Jia, L. Liu, and G. Fang, The finite-conducting ground's effect on the inductance of a rectangular loop, *J. Sens.* **2016**, 2765812 (2015).